ADVANCED FUNCTIONAL MATERIALS
www.afm-journal.de

Stabilization of Oxygen-Dependent $Fe^{3+/4+}$ Redox in Li-Excess DRX Cathode Exhibiting Anionic Redox via Transition Metal Combination

*Hayeon Lee, Minji Kim, Hyunyoung Park, Yiseul Yoo, Sangmun Na, Hee-Dae Lim, Jongsoon Kim, and Won-Sub Yoon**

Developing sustainable Li-ion batteries requires high-energy cathodes based on low-cost, earth-abundant elements, moving away from low-reserve nickel and cobalt. Fe-based oxide cathodes with $Fe^{3+/4+}$ and $O^{2-/n-}$ redox couples offer potential but face low initial Coulombic efficiency and significant voltage hysteresis. This study investigates Li-excess Fe-based disordered rock-salt (DRX) oxyfluorides ($Li_2Fe_{0.5}M_{0.5}O_2F$; M = Fe, Ti, Mn) using combined electrochemical/spectroscopic characterization and first-principles calculation. Oxygen-dependent $Fe^{3+/4+}$ redox, related to Fe 3d–O 2p hybrid state, can be stabilized when combined with $Mn^{3+/4+}$ redox in DRX structure owing to the unusual decrease in its redox potential. The moderately high charge transfer gap stabilizes Fe^{4+} against ligand-to-metal charge transfer (LMCT) on charge, reduces the amount of oxygen oxidation, thereby increasing Coulombic efficiency. On discharge, it allows metal-to-ligand charge transfer (MLCT) without substantial overpotential, reducing hysteresis in oxygen redox. The resulting composition exhibits high capacity (309 mAh g^{-1}) and energy density (998 Wh kg^{-1}), providing insights for next-generation Ni- and Co-free cathode materials.

1. Introduction

Global concerns about climate change have sparked a worldwide interest in renewable power generation and electric vehicles.[1] Li-ion batteries form a crucial component of these technologies, with significant efforts directed toward improving their energy density and reducing cost.[2,3] However, essential materials that optimally satisfy both parameters are still scarce, especially in the case of cathode materials.

Despite its low-cost, abundance, and environmental benignness, the use of Fe in cathode materials has been largely limited to olivine $LiFePO_4$,[4] which suffers from a low energy density. Attempts to utilize $LiFeO_2$ polymorphs as cathode materials[5,6] have been hindered by significant voltage hysteresis in the initial cycle and subsequent low operation voltages during charge/discharge. This issue is thought to stem from the unstable Fe^{4+} created during the first charge, which is reduced to Fe^{3+} during the same charge, thereby activating the less practical low-voltage $Fe^{2+/3+}$ redox couple in subsequent cycles.[5,7,8] The limitations of $LiFeO_2$ have driven researchers to explore new Fe-based cathode materials. Although the stabilization of Fe^{4+} during charging was observed in $LiNi_{0.9}Fe_{0.1}O_2$, increasing Fe content in the $LiNi_{1-x}Fe_xO_2$ chemical space led to a significant decrease in reversible capacity.[9,10] More promising Fe-based cathode materials were found among Li-excess systems that exhibit oxygen redox activity, such as $Li_{1.2}Mn_{0.4}Fe_{0.4}O_2$ ($0.5Li_2MnO_3$–$0.5LiFeO_2$),[11–13] $Li_{1.2}Ti_{0.4}Fe_{0.4}O_2$ ($0.5Li_2TiO_3$–$0.5LiFeO_2$),[14,15] $Li_{1.3}Nb_{0.3}Fe_{0.4}O_2$ ($0.43Li_3NbO_4$–$0.57LiFeO_2$),[16,17] Li_4FeSbO_6,[18,19] and Li_5FeO_4.[20,21] Many of these materials show high capacities of over 200 mAh g^{-1}. However, they still suffer from several issues, including low initial Coulombic efficiency, substantial voltage hysteresis, and inadequate cyclability. Addressing these challenges requires a deeper understanding of the combined

H. Lee, M. Kim, H. Park, S. Na, J. Kim, W.-S. Yoon
Department of Energy Science
Sungkyunkwan University
Suwon 16419, Republic of Korea
E-mail: wsyoon@skku.edu

Y. Yoo
Energy Storage Research Center
Korea Institute of Science and Technology (KIST)
Seoul 02792, Republic of Korea

H.-D. Lim
Department of Chemical Engineering
Hanyang University
Seoul 04763, Republic of Korea

J. Kim, W.-S. Yoon
SKKU Institute of Energy Science and Technology (SIEST)
Sungkyunkwan University
Suwon 16419, Republic of Korea

The ORCID identification number(s) for the author(s) of this article can be found under https://doi.org/10.1002/adfm.202312401

DOI: 10.1002/adfm.202312401

cationic/anionic redox process, a topic that is still under debate due to its complex operational mechanisms.[17,22–27] In the aforementioned Li-excess Fe-based cathode materials, the transition metal (TM) composition typically consists of either Fe^{3+} alone[20,21] or a combination of Fe^{3+} and high-valent cations (e.g., Mn^{4+},[11–13] Ti^{4+},[14,15] Nb^{5+},[16,17] and Sb^{4+}.[18,19]) that cannot be further oxidized during charging. Consequently, their initial charging proceeds with $Fe^{3+/4+}$ and $O^{2-/n-}$ ($n < 2$) oxidation. However, it remains unclear under which conditions the $Fe^{3+/4+}$ and $O^{2-/n-}$ redox processes can be stabilized to achieve high reversible capacity at moderately high voltages in close-packed oxides.[13,14,17,19–21,28,29] In particular, the characteristics of these redox processes across different compositions and their impact on electrochemical behaviors have not been systematically investigated within a uniform crystal structure.

In this study, we synthesized a series of Fe-based, earth-abundant cathode materials with three distinct TM combinations Fe–Fe, Fe–Ti, and Fe–Mn, using the mechanochemical method. These target cathode materials were based on the disordered rock-salt (DRX) structure, with partial substitution of oxygen anions by fluorine anions. This process resulted in unique compositional variations while maintaining the overall crystal structure. These materials demonstrated systematically differing initial Coulombic efficiencies and voltage hysteresis behaviors, the electronic structural origins of which were explored through a combination of electrochemical and spectroscopic characterizations, as well as computational simulations based on first-principles calculations. Our findings reveal that the TM combination in the DRX structure significantly influences the stabilization of the oxygen-dependent-redox (OD-redox) of $Fe^{3+/4+}$ and determines the reversibility of the anionic redox of $O^{2-/n-}$, which includes charge/discharge voltage hysteresis. We believe that this research provides valuable insights into stabilizing the $Fe^{3+/4+}$ and $O^{2-/n-}$ dual redox process, a crucial step in developing novel high-energy cathodes. Additionally, our findings contribute to a unified understanding of the anionic redox reaction in common Li-excess cathode materials.

2. Results and Discussion

2.1. Characterization of As-Prepared Materials

To explore compositional effects on the performance and reaction mechanism of Fe-based DRX cathodes, we designed $Li_2Fe_{0.5}M_{0.5}O_2F$ (M = Fe,[30] Ti, Mn) (1:1 combination of LiF and $LiFe_{0.5}M_{0.5}O_2$). These samples, with M = Fe, Ti, and Mn, are hereafter denoted as LFOF, LFTOF, and LFMOF, respectively. LiF was used as the Li-excess component to facilitate Li^+ diffusion in the DRX cathodes.[31,32] To attain heavy fluorination (≈33% of total anions), a mechanochemical ball-milling method was used for sample synthesis.[33] All samples were synthesized under the same conditions, except for their compositions, to conduct a comparative study (see details in the Experimental Section). The inductively coupled plasma atomic emission spectroscopy (ICP-AES) results show that the metal ratios in the as-prepared materials align well with the theoretical ratios (Table S1, Supporting Information). As depicted in the energy-dispersive spectroscopy (EDS) maps, all the constituent elements are homogeneously distributed at the particle level for all samples (Figure S1, Supporting Information). Rietveld refinements performed on the X-ray diffraction (XRD) patterns of the samples (**Figure 1a–c**; Table S2a–c, Supporting Information) reveal that they form a single DRX phase (S.G. Fm-3m) with lattice constants of a = 4.155, 4.162, and 4.154 Å for LFOF, LFTOF, and LFMOF, respectively. Line broadening analysis based on the Scherrer equation reveals a mean crystallite size of 58, 53, and 46 Å for LFOF, LFTOF, and LFMOF, respectively. As confirmed by transmission electron microscope (TEM) analysis, the primary particles are between 20–50 nm in size and polycrystalline (Figure S2, Supporting Information). The soft X-ray absorption spectroscopy (XAS) spectra of the three samples at the F K-edge (Figure S3, Supporting Information) exhibit dominant signatures of LiF, implying that many F ions exist in the Li-excess (LiF-like) local environment, aligning with theoretical expectations.[34] However, features corresponding to F—TM bonds are also detected in the spectra, indicating that some O ions in the TM precursors were indeed replaced by F ions during the mechanochemical synthesis. Scanning electron microscope (SEM) observations (Figure S4, Supporting Information) show that the primary particles of the as-prepared samples form agglomerates of varying sizes. These agglomerates are further pulverized into uniform carbon-active material mixtures after ball-milling with carbon for electrode fabrication. The X-ray absorption near edge structure (XANES) spectroscopy (Figure S5, Supporting Information) identifies the oxidation states of TM ions in the as-prepared materials to be close to Fe^{3+} in LFOF, Fe^{2+}-Ti^{4+} in LFTOF, and Fe^{3+}-Mn^{3+} in LFMOF. These oxidation states are preserved after electrode fabrication. The theoretical capacity reservoirs of the samples are provided in Table S3 (Supporting Information).

2.2. Electrochemical Behaviors

Figure 1d–f presents the voltage profiles of LFOF, LFTOF, and LFMOF electrodes over the first three cycles, at a current density of 20 mA g^{-1} between 1.5 and 4.8 V. Remarkably large initial charge capacities are observed: 344, 325, and 328 mAh g^{-1}, corresponding to the extraction of 1.55, 1.42, and 1.47 Li per formula unit (f.u.) for LFOF, LFTOF, and LFMOF, respectively. These values significantly exceed the theoretical TM-related capacities of each material (Table S3, Supporting Information), suggesting potential anionic redox activity in all of them. However, systematic differences are observed in the electrochemical behavior of each material in terms of the first-cycle Coulombic efficiency and voltage hysteresis. LFOF exhibits a very low first-cycle Coulombic efficiency of 60.8%, with a first discharge capacity of 209 mAh g^{-1} (specific energy of 573 Wh Kg^{-1}), corresponding to the insertion of 0.94 Li per f.u. LFOF also displays significant voltage hysteresis between the first charge and discharge profiles, with a voltage gap of ≈1.5 V persisting in subsequent cycles, excluding the low voltage charge/discharge region below 3 V, which appears only after the irreversible first charge process. LFTOF displays a superior first-cycle Coulombic efficiency of 88.6% compared to LFOF, with a first discharge capacity of 288 mAh g^{-1} (specific energy of 780 Wh kg^{-1}), representing the insertion of 1.25 Li per f.u. However, a substantial voltage hysteresis of ≈1.5 V, similar to LFOF, is still observed. Among the samples, LFMOF performs the best, displaying the highest first-cycle Coulombic efficiency of 94.2%

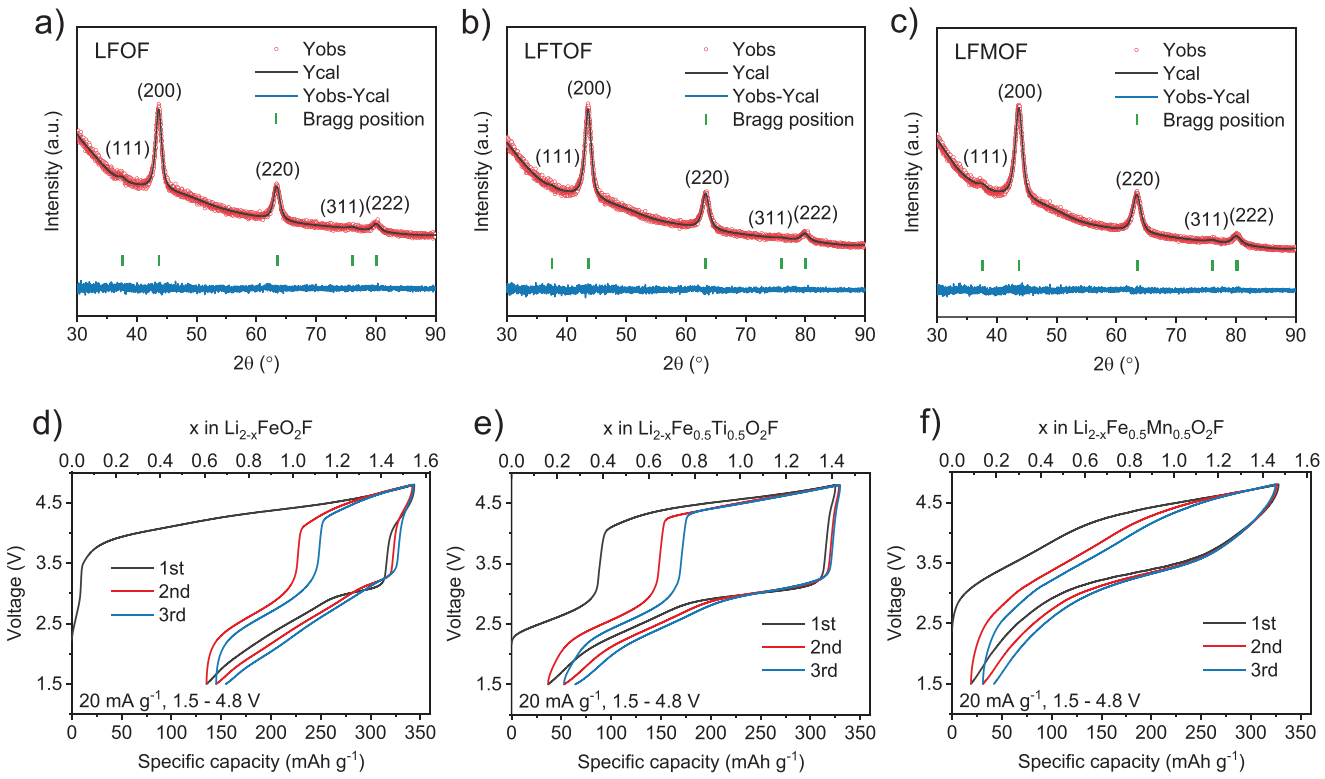

Figure 1. As-prepared structures and electrochemical behaviors. Rietveld refinement analyses on XRD patterns of as-prepared powder samples. a) LFOF, b) LFTOF, and c) LFMOF. Voltage profiles of d) LFOF, e) LFTOF, and f) LFMOF electrodes for initial three cycles, at a current density of 20 mA g^{-1} between 1.5 and 4.8 V. Cycling tests were performed at room temperature (≈25 °C).

and the lowest voltage hysteresis of ≈0.9 V. It also delivers the highest first discharge capacity of 309 mAh g^{-1} (specific energy of 998 Wh Kg^{-1}), corresponding to the insertion of 1.39 Li per f.u. These systematic differences in the initial Coulombic efficiency and voltage hysteresis among the samples prompted us to delve deeper into their respective redox mechanisms. In particular, we hypothesized that these two characteristics are strongly tied to the nature of the anionic redox process, as seen in several other Li-excess cathode materials.[17,22–25,35] The differential electrochemical mass spectrometry (DEMS) results of the three samples (Figure S6, Supporting Information) reveal a significant O_2 release only in LFOF at the end of the first charge, suggesting that the anionic redox process in LFTOF and LFMOF may be more reversible than that in LFOF. The redox mechanisms of each sample were further investigated through a combination of electrochemical and spectroscopic methods, as detailed below.

2.3. Redox Mechanism of LFOF

Figure 2a,b displays the voltage profiles and corresponding dQ/dV curves of LFOF for the first cycle under various charge cut-off conditions. The first charge process consists of two faintly separated regions: i and ii. When the charge cut-off capacities are limited up to 110 mAh g^{-1} (region i), slope discharge profiles corresponding to broad dQ/dV curves are observed. A magnified view of the dQ/dV curves (Figure S7, Supporting Information) reveals that subtle multiple discharge processes emerge within this cut-off range. Further charging beyond 110 mAh g^{-1} (region ii) induces a more noticeable hysteretic reduction feature in the middle of discharge, dividing the discharge process into three distinct regions (iii, iv, and v). The discharge capacities of regions iii and iv suddenly decreases when the charge cut-off is raised above 165 and 275 mAh g^{-1}, respectively. However, the discharge capacity of region v continuously increases as the charge cut-off level is increased up to 4.8 V (see also Figure S8, Supporting Information).

To investigate the detailed redox reactions involved in each region, XAS was employed. Figure 2c presents the ex situ XANES spectra of LFOF at the Fe K-edge during the first cycle and the second charge process. Figure 2d displays the evolution of the Fe—O/F bond distance derived from the first shell fitting on the Fe K-edge extended X-ray absorption fine structure (EXAFS) spectra. Both XANES and EXAFS analyses were performed for the same ex situ sampling points marked in the bottom panel of Figure 2d. During the first charge process, the Fe K-edge XANES spectra do not show any considerable shift from the position of Fe_2O_3, but certain changes in the white line shape at ≈7132 eV are noticeable. If the electrons had been primarily extracted from the Fe 3d states during charging, the increased effective nuclear charge would have necessitated more energy for the excitation of core electrons, resulting in a rigid edge shift toward higher energy. However, this is not observed in the results, suggesting that there is no predominant "cation-centered" oxidation of Fe^{3+}. It should be noted that there is a noticeable decrease in the Fe—O/F bond distance during the first charge

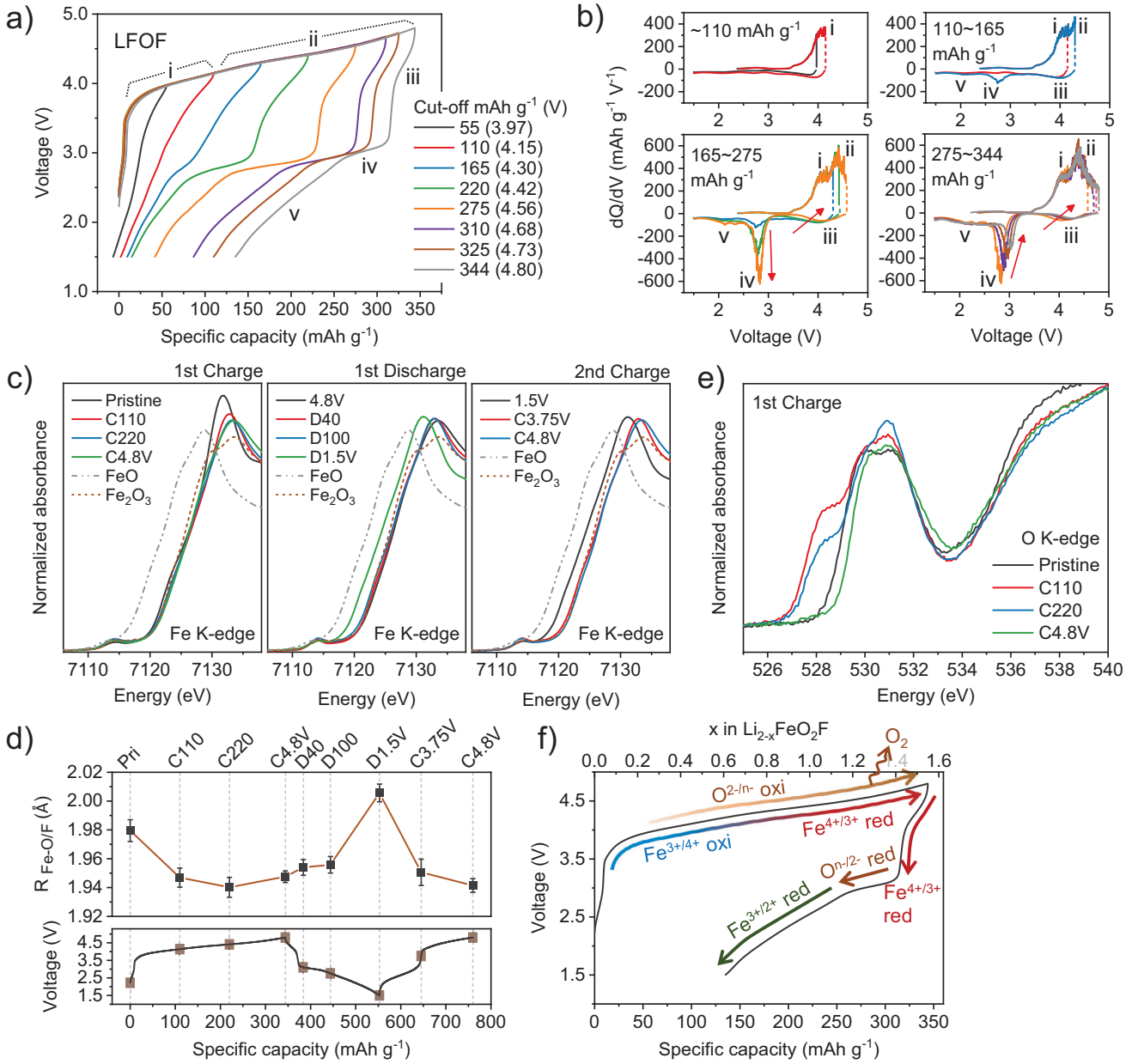

Figure 2. Redox mechanism of LFOF. a) First-cycle voltage profiles with different charge cut-off values and b) their dQ/dV curves. Same color coding is used in (a) and (b). c) Normalized ex situ Fe K-edge XANES spectra. d) Fe—O/F bond distances derived from EXAFS fitting at Fe K-edge (upper panel; the fits to the data and detailed fitting results are shown in Figure S9 and Table S4, Supporting Information, respectively), and voltage profiles providing trace of corresponding charge/discharge states (bottom panel). e) Normalized ex situ O K-edge XAS spectra in FY mode. f) Schematic illustration of redox mechanism of LFOF.

process. Combining this with the XANES results suggests that electron extraction has occurred within the Fe—O/F bond, but more biased toward the ligand side. Given that anionic redox is known to involve local distortion rather than direct changes in the collective bond distance,[23,27,36] the ligand hole is most likely to be present within the Fe 3d–O/F 2p hybridized state (primarily on the O side due to the high electronegativity of F). For simplicity, the redox process involving such changes in the Fe—O/F bond distance occurring beyond the Fe^{3+} limit will be referred as "oxygen-dependent-redox (OD-redox)" of $Fe^{3+/4+}$ throughout this paper. In more detail, for the first charge process, the Fe—O/F bond distance largely decreases in the early stage (0–110 mAh g^{-1}), but the decrement becomes small in the later stage (110–220 mAh g^{-1}) and is followed by rather increase in the distance at the end of the charge (220 mAh g^{-1}–4.8 V). This indicates that the OD-oxidation of Fe^{3+} initially occurs, but its amount decreases upon continued charging, and the OD-oxidized Fe^{4+} is finally reduced. Given that Fe is the only TM

element in LFOF, the above results suggest that oxygen oxidation occurs in this material, gradually increasing its capacity contribution and finally being over-activated to generate surplus electrons being redistributed into the Fe—O/F bonds without contributing to the charge capacity. This behavior can be attributed to the oxygen oxidation process involving ligand-to-metal charge transfer (LMCT),[19,37] and it clearly indicates that Fe^{4+} is unstable in LFOF during charging. Turning to the first discharge process, the Fe K-edge XANES spectra show negligible variations for the initial discharging (4.8 V–100 mAh g^{-1}). However, the Fe—O/F bond distance in the same region shows a subtle but noticeable two-step variation: a certain increase at the beginning (4.8 V–40 mAh g^{-1}), followed by smaller changes (40–100 mAh g^{-1}). This implies that the two separate cathodic processes in regions iii and iv are mainly related to the $Fe^{4+/3+}$ OD-reduction and the $O^{n-/2-}$ reduction, respectively. These assignments are supported by DEMS analyses; O_2 release in LFOF occurs largely only above 4.5 V (Figure S6a, Supporting Information), which corresponds well with the sharp decrease in the capacity of region iv after raising the charge cut-off voltage above 4.56 V (275 mAh g^{-1}) (Figure 2a,b; Figure S8, Supporting Information). In the following discharging (100 mAh g^{-1}–1.5 V), a rigid shift of the Fe K-edge XANES spectra toward the position of the FeO reference and a significant increase of Fe—O/F bond distance clearly indicate that $Fe^{3+/2+}$ reduction occurs during the low-voltage discharging (region v). Consequently, the low-voltage $Fe^{2+/3+}$ oxidation newly appears in the second charge process (1.5–3.75 V), which can also be corroborated by the rigid XANES edge shift and a significant decrease in the Fe—O/F bond distance. At the end of the second charge process (3.75–4.8 V), the Fe K-edge XANES spectra show minimal variations, but a certain decrease in the Fe–O/F distance implies that some amount of $Fe^{3+/4+}$ OD-oxidation occurs. It likely also accompanies some amount of oxygen oxidation, as evidenced by the existence of two reduction features corresponding to regions iii ($Fe^{4+/3+}$ OD-reduction) and iv ($O^{n-/2-}$ reduction) in the second discharge (see Figure 1d).

To understand the irreversible first charge process in more detail, the activation process of the oxygen redox was further investigated by soft XAS. Figure 2e shows the ex situ soft XAS spectra of LFOF at the O K-edge, measured in the bulk-sensitive fluorescence yield (FY) mode for the first charge process. The pre-edge region below 534 eV is primarily associated with the electron transition from O 1s to the unoccupied Fe 3d–O 2p hybridized states. Before charging, a double peak feature observed between the 529–532 eV range can be attributed to the Fe^{3+}–O hybridized states.[38,39] Charging to 110 mAh g^{-1}, however, generates a new peak at ≈528.3 eV. This peak can be related to the formation of Fe^{4+} involving significant ligand (oxygen) hole character.[40] Although these types of O holes emerges within the Fe–O hybridization, O holes can also be created in non-bonding (unhybridized) O 2p states.[26] These are unstable and may consequently form more stable short O–O species (peroxide-like dimer,[41] O_2 molecule,[25,42] etc.). This process is often called "anionic (oxygen) redox".[24,26] In this respect, it can be noticed that another peak at ≈531 eV gaining certain spectral weight in the early charging stage (0–110 mAh g^{-1}). This is a representative feature observed in the O K-edge spectra of Li_2O_2[43] and O_2,[44] and has been observed in Li-excess cathodes as a result of oxygen oxidation.[17,45] During the following charging (110–220 mAh g^{-1}), the intensity of the 531 eV peak is further increased, but that of the 528.3 eV peak is rather decreased. This suggests that oxygen oxidation increases while Fe^{4+} is reduced to Fe^{3+} by LMCT. At the end of the charging (220 mAh g^{-1}–4.8 V), both peaks significantly lose their intensities, indicating that the Fe^{4+} and O^{n-} states largely disappear due to LMCT and O_2 release. The O K-edge XAS results support the occurrence of oxygen redox in LFOF, although it is quite irreversible when the upper cut-off voltage is 4.8 V. The oxygen oxidation in this sample appears to begin in the early stage of charging before 110 mAh g^{-1}, although corresponding reduction feature (region iv) is not explicitly seen in the voltage opening experiment (Figure 2a,b), likely due to its burial within complex multiple reduction features (Figure S7, Supporting Information). Indeed, the fact that the oxidation processes of Fe^{3+} and O^{2-} are subject to overlap can be readily expected from the proximity of regions i ($Fe^{3+/4+}$ OD-oxidation) and ii ($O^{2-/n-}$ oxidation) in narrow voltage ranges (Figure 2b). Based on the electrochemical and spectroscopic information obtained above, the first-cycle redox mechanism of LFOF is depicted schematically in Figure 2f.

2.4. Redox Mechanism of LFTOF

Figure 3a,b displays the voltage profiles and corresponding dQ/dV curves of LFTOF for the first cycle under different charge cut-off conditions. The first charge starts with a low-voltage oxidation process (region I) followed by two high-voltage regions weakly separated from each other (regions II and III). When charging to 3.5 V, a well-defined low-voltage reduction process is observed (region VI). However, further charging into the high-voltage region induces two notably separate reduction processes, at above 4 V and at ≈3 V, the latter of which shows significant hysteresis. This results in the overall discharge process being divided into three different regions (IV, V, and VI). The discharge capacity of region IV initially increases but drops suddenly when the charge cut-off level is raised above 200 mAh g^{-1}, while that of region V gradually increases as the charge cut-off level is increased up to 4.8 V. For region VI, the discharge capacity slightly increases as the cut-off level rises.

To investigate the detailed redox processes involved in each region, XAS was utilized. Figure 3c shows the ex situ XANES spectra of LFTOF at the Fe K-edge during the first cycle and the second charge process. Figure 3d displays the evolution of the Fe—O/F bond distance derived from the first shell fitting on the Fe K-edge EXAFS spectra. Both XANES and EXAFS analyses were performed for the same ex situ sampling points marked in the bottom panel of Figure 3d. During the first charge process, the Fe K-edge XANES spectra at the low-voltage region (0–3.5 V) show a rigid edge shift from the position of FeO to that of Fe_2O_3. Concurrently, a significant decrease in the Fe—O/F bond distance is observed in the same region, clearly indicating that $Fe^{2+/3+}$ oxidation occurs during low-voltage charging. In the following high-voltage charge process (3.5–4.8 V), the Fe K-edge XANES spectra show no significant variation. However, the Fe—O/F bond distance in the same region shows a certain decrease at the beginning (3.5 V–200 mAh g^{-1}), followed by a slight increase (200 mAh g^{-1}–4.8 V; see Figure 3e). This suggests that some OD-oxidation of Fe^{3+} initially occurs in the high-

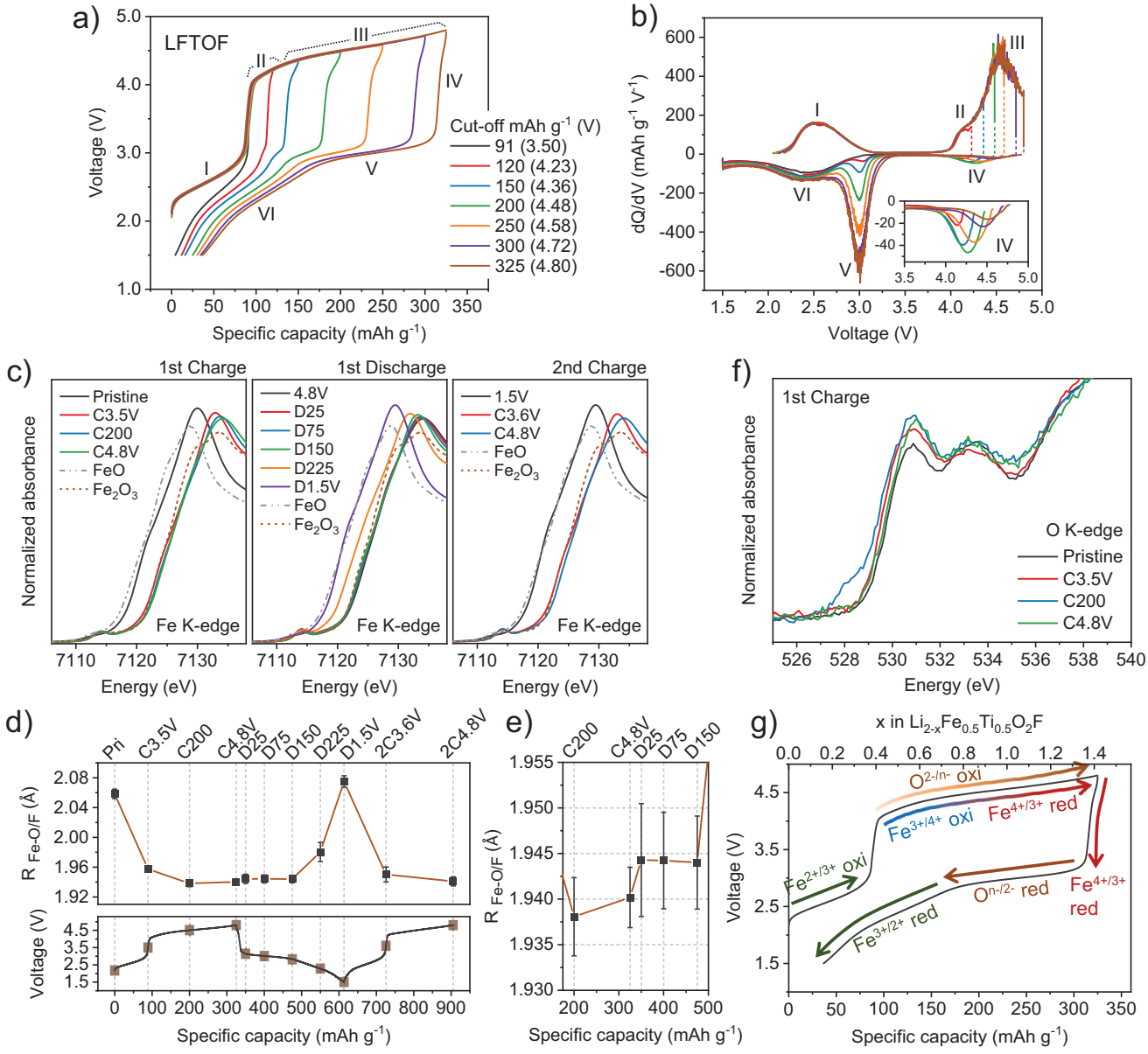

Figure 3. Redox mechanism of LFTOF. a) First-cycle voltage profiles with different charge cut-off values and b) their dQ/dV curves. Same color coding is used in (a) and (b). c) Normalized ex situ Fe K-edge XANES spectra. d) Fe—O/F bond distances derived from EXAFS fitting at Fe K-edge (upper panel; the fits to the data and detailed fitting results are shown in Figure S10 and Table S5, Supporting Information, respectively), and voltage profiles providing trace of corresponding charge/discharge states (bottom panel). e) A magnified view of Fe—O/F bond distance from C200 of first charge to D150 of first discharge. f) Normalized ex situ O K-edge XAS spectra in FY mode. g) Schematic illustration of redox mechanism of LFTOF.

voltage region, but its amount decreases upon continued charging, and finally, the OD-oxidized Fe^{4+} is reduced. In LFTOF, Ti^{4+} remains inactive throughout the first cycle and the second charge processes (Figure S11, Supporting Information). This implies that oxygen oxidation occurs in LFTOF during charging in the high-voltage region, gradually increasing its capacity contribution, and finally, some electrons produced by the oxygen oxidation are redistributed into the Fe—O/F bonds without contributing to the charge capacity. This behavior indicates that like in LFOF, Fe^{4+} in LFTOF is unstable against LMCT during charging. Turning to the first discharge process, whereas the Fe K-edge XANES spectra show only minor variations during discharging to 150 mAh g^{-1}, the Fe—O/F bond distance in the same region displays a subtle but meaningful two-step variation: a slight increase at the beginning (4.8 V–25 mAh g^{-1}), followed by negligible changes (25–150 mAh g^{-1}) (Figure 3e). These results imply that a small amount of $Fe^{4+/3+}$ OD-reduction may occur during the initial discharge (region IV), whereas the following discharge up to 150 mAh g^{-1} (region V) is dominated by $O^{n-/2-}$ reduction. In the low-voltage discharge process (150 mAh g^{-1}–1.5 V), a rigid shift of the Fe K-edge XANES spectra toward the position of FeO, along with a significant increase in the Fe—O/F bond distance,

clearly shows that $Fe^{3+/2+}$ reduction occurs (region VI). The assignment of region IV as $Fe^{4+/3+}$ OD-reduction can be supported by the sudden decrease in its discharge capacity observed in the voltage opening experiment when the charge cut-off condition is raised above 200 mAh g^{-1} (Figure 3a,b). Because this decrease coincides with an increase in the Fe—O/F bond distance (i.e., $Fe^{4+/3+}$ OD-reduction) during charging (Figure 3e). Given the relatively rigid spectroscopic evidence of region VI as $Fe^{3+/2+}$ reduction (and the inactivity of Ti^{4+} as well), it is reasonable to assign region V as "$O^{n-/2-}$ reduction". Indeed, the gradual increase in region V upon increasing charge cut-off level (Figure 3a,b) aligns well with the negligible O_2 loss observed by DEMS (Figure S6b, Supporting Information), further supporting our assignments. In the second charge process, the Fe K-edge XANES spectra and the Fe—O/F bond distance show similar behaviors to those of the first charge process, implying that oxidation reactions of Fe^{2+} and Fe^{3+} occurred at the low- and high-voltage regions, respectively. There will also be $O^{2-/n-}$ oxidation at the high-voltage region, as evidenced by the existence of a long discharge plateau in the second discharge process (see Figure 1e).

To clearly understand the activation process of the oxygen redox in LFTOF, Figure 3f depicts the ex situ soft XAS spectra at the O K-edge in the FY mode for the first charge process. In the pre-edge region below 535 eV (unoccupied Fe 3d–/Ti 3d–O 2p hybridized states), two peaks observed before charging, centered at ≈530.8 and 533.5 eV, can be attributed to the superposition of Fe^{2+}–/Ti^{4+}–O hybridized states. Referring to the reported O K-edge spectra of FeO and TiO_2, Fe^{2+}–O contribution is primarily on the peak at lower energy, but Ti^{4+}–O contributes to both peaks.[39,46] Upon charging to 3.5 V, the peak at lower energy gains certain intensity, which may be related to the formation of Fe^{3+}, given that both the Fe^{2+}–O and Fe^{3+}–O contributions exist at a similar energy range between 529–532 eV.[39,46] As the charging continues at the high-voltage region up to 200 mAh g^{-1}, additional intensity gains are observed at ≈528.3 and 531 eV. These are similar to those observed in LFOF (Figure 2e) and can be associated with the formation of Fe^{4+} and oxidized oxygen (O^{n-}) ions, respectively. At the 4.8 V level, the intensity of the 528.3 eV peak significantly decreases, while the intensity of the 531 eV peak remains high. These results clearly demonstrate that in LFTOF, the O^{n-} state is stable up to 4.8 V, even though Fe^{4+} is unstable against LMCT, resulting in OD-reduction back to Fe^{3+}. Based on the electrochemical and spectroscopic information gathered, the first-cycle redox mechanism of LFTOF is depicted schematically in Figure 3g.

2.5. Redox Mechanism of LFMOF

Figure 4a,b displays the evolution of voltage profiles and the corresponding dQ/dV curves of LFMOF according to different charge cut-off conditions. The charge voltage profile comprises two different slope regions that correlate with two oxidation processes in dQ/dV curves (regions [i] and [ii]). Charging between 0 and 160 mAh g^{-1} (region [i]) yields symmetric charge/discharge profiles without significant voltage hysteresis. However, further charging beyond 160 mAh g^{-1} (region [ii]) induces a hysteretic reduction reaction at ≈3.3 V, dividing the overall discharge process into three regions ([iii], [iv], and [v]). Contrary to LFOF and LFTOF, a decrease in the capacity of a certain reduction process as the cut-off level increases, is not observed in LFMOF, suggesting more reversible redox reactions during the first cycle.

Detailed redox processes in each region were examined using XAS. Figure 4c presents the ex situ XANES spectra of LFMOF at the Fe K-edge during the first cycle and the second charge process, and Figure 4d shows the evolution of Fe—O/F bond distance derived from the first shell fitting on the Fe K-edge EXAFS spectra. Both XANES and EXAFS analyses were performed for the same ex situ sampling points, as marked in the bottom panel of Figure 4d. Throughout the first cycle and second charge process, the Fe K-edge XANES spectra exhibit reversible changes in the white line shape at ≈7132 eV, implying that Fe^{3+} ions in LFMOF are reversibly oxidized and reduced during the charge/discharge process. This can be further corroborated by the changes in Fe—O/F bond distance. During the first charge process, the Fe—O/F bond distance clearly decreases until charging to 160 mAh g^{-1} (region [i]) followed by negligible changes up to 4.8 V (region [ii]), indicating that $Fe^{3+/4+}$ OD-oxidation occurs in the first slope region. Turning to the first discharge process, the Fe—O/F bond distance continuously increases with a slight delay in the 75–150 mAh g^{-1} region ([iv]), implying that $Fe^{4+/3+}$ OD-reduction occurs throughout the first discharge, except for the middle stage where the reaction temporarily slows down. In the second charge process, the Fe—O/F bond distance variation mirrors that observed in the first charge process, suggesting that $Fe^{3+/4+}$ OD-redox is highly stabilized in LFMOF. Additionally, the redox process of Mn ions was investigated by XAS (combined XANES and EXAFS analyses), and the presence of reversible $Mn^{3+/4+}$ redox reactions is definitively confirmed (Figure S13, Supporting Information). Interestingly, it is found that the $Mn^{3+/4+}$ redox reaction in LFMOF occurs almost in the same region as the $Fe^{3+/4+}$ redox reaction, implying the coupling of both redox reactions in LFMOF.

To clearly understand the activation process of the oxygen redox in LFMOF, we analyzed the ex situ soft XAS spectra at the O K-edge in the FY mode for the first charge process (Figure 4e). In the pre-edge region below 534 eV (unoccupied Fe 3d–/Mn 3d–O 2p hybridized states), broad multiple peaks between 528–534 eV range are observed before charging, a result of the superposition of Fe^{3+}–O and Mn^{3+}–O hybridized states. During charging to 160 mAh g^{-1}, significant spectral weight gains appear at ≈529.7 eV. A similar feature has been observed in Mn-containing DRX cathodes during $Mn^{3+/4+}$ oxidation.[47,48] Notably, the spectral feature at ≈528.3 eV observed in LFOF and LFTOF (Figures 2e and 3f) is absent in LFMOF despite the coexistence of OD-oxidation from Fe^{3+} to Fe^{4+} in this charging range. This suggests that the spectral weight corresponding to the Fe^{4+} state is formed at higher energy and merged into the Mn^{4+} feature, a point we will discuss further later in the paper. In the following charge process (160 mAh g^{-1}–4.8 V), an additional intensity gain at ≈531 eV is observed. Similar to that in LFOF and LFTOF (Figures 2e and 3f), this peak can be attributed to the oxygen oxidation (O^{n-}). Throughout the first charge process, there is no notable spectral weight loss at the 529.7 and 531 eV peaks, suggesting that the Fe^{4+}, Mn^{4+}, and O^{n-} states are largely stabilized in LFMOF. Based on the electrochemical and spectroscopic information acquired, we summarize the first-cycle redox mechanism, which is schematically depicted in Figure 4f.

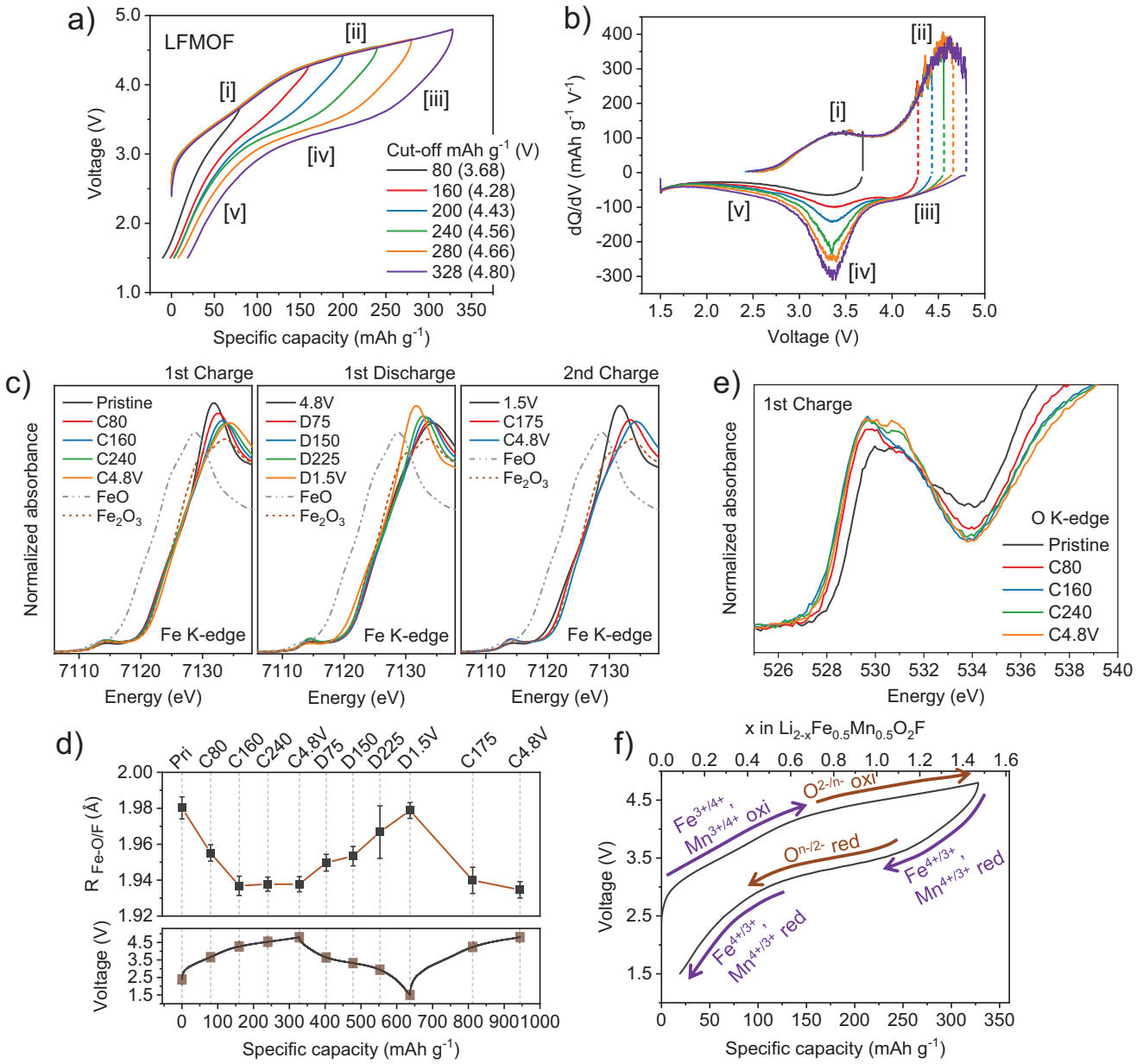

Figure 4. Redox mechanism of LFMOF. a) First-cycle voltage profiles with different charge cut-off values and b) their dQ/dV curves. Same color coding is used in (a) and (b). c) Normalized ex situ Fe K-edge XANES spectra. d) Fe—O/F bond distances derived from EXAFS fitting at Fe K-edge (upper panel; the fits to the data and detailed fitting results are shown in Figure S12 and Table S6, Supporting Information, respectively), and voltage profiles providing trace of corresponding charge/discharge states (bottom panel). e) Normalized ex situ O K-edge XAS spectra in FY mode. f) Schematic illustration of redox mechanism of LFMOF.

2.6. Theoretical Investigation on the Evolution of Hole States

Further investigations using first-principles calculation were performed to verify the evolution of hole states upon Li^+ deintercalation. **Figure** 5a–c presents the projected density of states (pDOS) of the samples calculated at various states of charge. As depicted in Figure 5a, the pristine state of LFOF displays high electron density for the hybridized Fe 3d–O 2p state near the Fermi level, marked in yellow. During Li^+ deintercalation, they oxidize, donating electrons and resulting in a change in hole density, marked in blue. It is evident that the hole portion of the O 2p orbital in the hybridized Fe 3d–O 2p state of LFOF is enlarged with an increase in Li^+ deintercalation content, implying the formation of a ligand hole instead of direct oxidation from Fe^{3+} to Fe^{4+}. For LFTOF (Figure 5b), initial deintercalation of 0.5 Li^+ causes significant holes in the Fe 3d orbital, corresponding to the rigid $Fe^{2+/3+}$ oxidation. However, further deintercalation results in a significant increase in the hole portion of the O 2p orbital in the hybridized Fe 3d–O 2p state, implying the formation of ligand holes instead. In the case of LFMOF (Figure 5c), the hybridized Fe/Mn 3d–O 2p

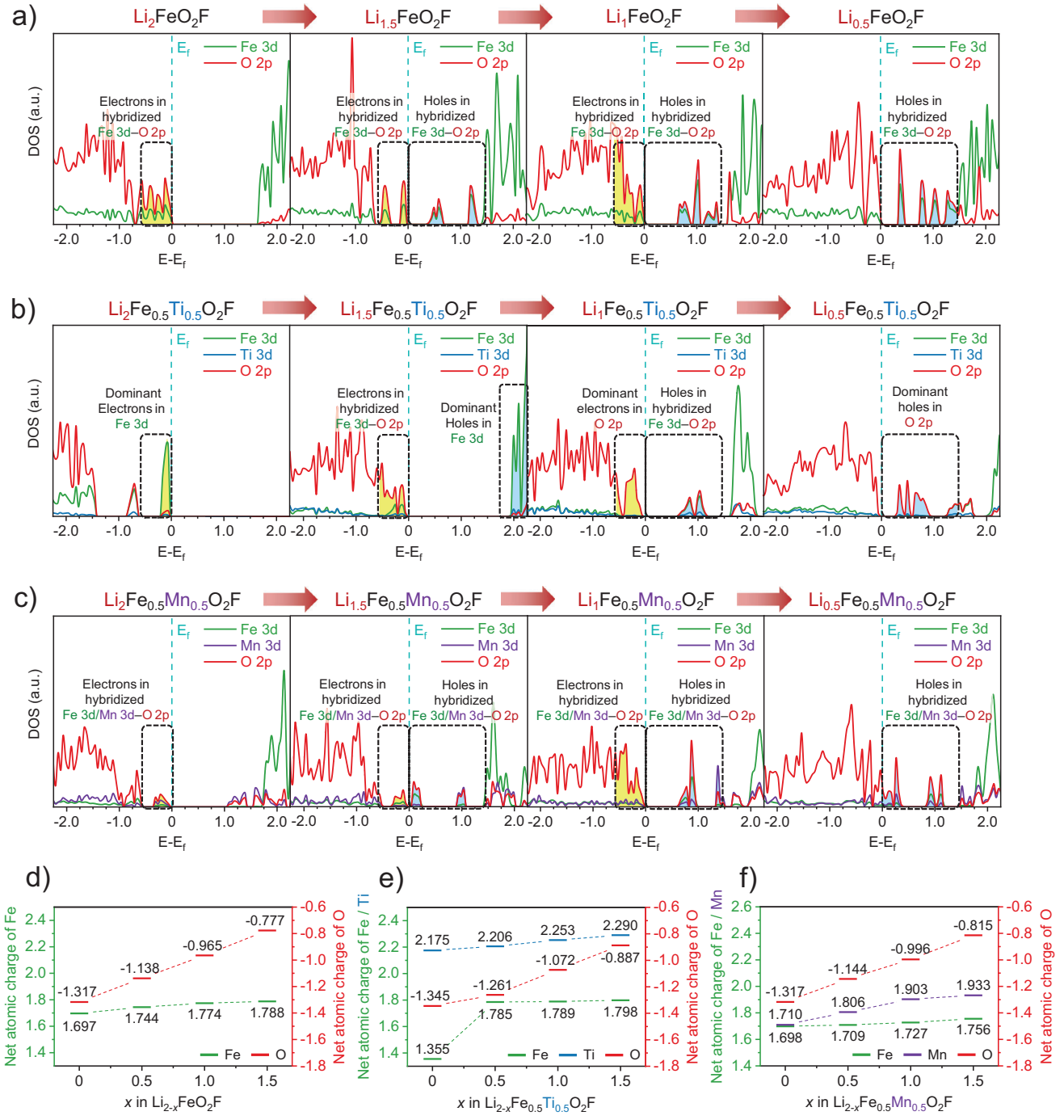

Figure 5. Theoretical investigation on evolution of hole states. pDOS of a) Fe 3d and O 2p orbitals in $Li_{2-x}FeO_2F$, b) Fe 3d, Ti 3d, and O 2p orbitals in $Li_{2-x}Fe_{0.5}Ti_{0.5}O_2F$, and c) Fe 3d, Mn 3d, and O 2p orbitals in $Li_{2-x}Fe_{0.5}Mn_{0.5}O_2F$. Bader charge analyses results for d) $Li_{2-x}FeO_2F$, e) $Li_{2-x}Fe_{0.5}Ti_{0.5}O_2F$, and f) $Li_{2-x}Fe_{0.5}Mn_{0.5}O_2F$. x = 0, 0.5, 1, and 1.5.

state simultaneously donates electrons. It is observed that there is a considerable difference in the hole properties of the Fe 3d–O 2p and Mn 3d–O 2p hybridized states. The hole portions primarily increase on the O 2p orbitals for the former, but there is a noticeable increase in the hole portion on the Mn 3d orbitals for the latter. These results indicate that oxidation of Fe^{3+} primarily creates ligand holes, whereas oxidation of Mn^{3+} induces a significant amount of TM d holes.

The characteristics of hole states were further verified using Bader charge analyses. As shown in Figure 5d,f, the net charge of the Fe element in LFOF and LFMOF experiences minimal variations during Li^+ deintercalation. However, the net charge of

the O element undergoes significant changes. Similar behaviors are also observed in LFTOF after 0.5 Li^+ deintercalation, which corresponds to the $Fe^{2+/3+}$ oxidation (Figure 5e). These results confirm that in all the samples, oxidation of Fe^{3+} induces ligand hole states rather than direct oxidation toward Fe^{4+}. Meanwhile, a gradual increase in the net charge of the Mn element in LFMOF during Li^+ deintercalation is observed, indicating the formation of d holes during the $Mn^{3+/4+}$ oxidation. Upon deintercalation of 1.5 mol Li^+, the net charge of the O element increases by 0.540, 0.458, and 0.502 for LFOF, LFTOF, and LFMOF, respectively. The increase in LFTOF is lower than that in LFOF due to the presence of $Fe^{2+/3+}$ oxidation with a strong d hole character. In the case of LFMOF, despite the increment being lower than in LFOF owing to the presence of $Mn^{3+/4+}$ oxidation, it is higher than in LFTOF. This is because the $Mn^{3+/4+}$ oxidation in LFMOF involves a higher ligand hole character than the $Fe^{2+/3+}$ oxidation in LFTOF. In anionic redox-based cathodes, high-valent TM ions with significant ligand hole character can induce internal charge redistribution, resulting in the transfer of holes from the TM–O hybridized state to oxidized oxygen.[22,23,49,50] This phenomenon was indeed experimentally observed for LFOF and LFTOF, where the OD-oxidized Fe^{4+} was reduced to Fe^{3+} by LMCT during charging, leaving behind an increase in the oxygen oxidation content. Ultimately, most of the net charge increase of oxygen in these two samples can be attributed to oxygen oxidation. However, as will be elaborated in the next section, even though the net charge increase of oxygen in LFMOF is higher than that in LFTOF, the oxygen oxidation content in LFMOF is virtually the smallest among the three samples when the same charging depth is applied. This is because, unlike LFOF and LFTOF, ligand hole states for Fe^{4+} (and Mn^{4+}) are significantly stabilized in LFMOF.

2.7. $Fe^{3+/4+}$ and $O^{2-/n-}$ Redox Reactions Depending on TM Combination, and Their Relevance with First-Cycle Coulombic Efficiency and Voltage Hysteresis

The comparison of redox mechanisms (Figures 2f, 3g, and 4f) shows that the $Fe^{3+/4+}$ OD-redox in LFMOF has two different electrochemical behaviors compared to those in LFOF and LFTOF. First, the OD-oxidation of Fe^{3+} in LFMOF (that happens simultaneously with the oxidation of Mn^{3+}) occurs at a much lower voltage than those in LFOF and LFTOF. Second, the OD-reduction of Fe^{4+} back to Fe^{3+} during charging is largely suppressed in LFMOF. The XAS analyses and the first-principles calculations confirmed that the local electronic structure of Fe^{4+} in all the samples is closer to $d^5\underline{L}$ than d^4 ($\underline{L}$: ligand hole).[40,51] This electronic structure is a known feature of 3d TM oxides composed of high-valent post-TM elements, such as Fe^{4+}, Ni^{3+}, and Cu^{3+}.[52–54] Although the samples in this paper are oxyfluorides (Li_2TMO_2F), the unoccupied Fe–O/F hybridized states near the Fermi level, which are associated with Fe^{4+}, may be dominated by O states, given strong electronegativity of F whose states must sit far below the O states. This rationalizes the use of O K-edge XAS for comparing the nature of $Fe^{3+/4+}$ OD-redox in our samples. Owing to the weak core-hole effect and the absence of strong electron correlation, the O K-edge XAS spectra of TM oxides can be considered a reasonable approximation of the unoccupied pDOS on O 2p orbital and can also be interpreted as the conduction band DOS due to the hybridization between TM 3d and O 2p orbitals.[55,56] Note that while we employed density functional theory (DFT) calculations in the previous chapter to investigate the characteristics of hole states, predicting the exact DOS using DFT calculations can be very challenging, particularly for the transition metal compounds. This is due to the presence of strong electron correlation, which often necessitates empirical treatments (e.g., Hubbard U parameter in DFT+U). This can result in significant deviations in the calculated results from the actual DOS.[24] Because of this uncertainty, we decided to use O K-edge XAS spectra as an experimental probe for the conduction band. The position of the lowest-energy peak in the pre-edge region of the O K-edge spectrum for oxide cathodes, which reflects the energy level of the lowest unoccupied TM 3d–O 2p hybridized states, can be related to the electrochemical potential, as previously verified for a wide range of TM(3d)-based oxide cathodes.[39] Moreover, since the non-bonding O 2p states, which are the particular states involved in oxygen redox reactions in the TM-based oxide cathodes, have relatively fixed energy levels regardless of the composition or structure,[26] the peak position can naturally be associated with the charge transfer gap between the lowest unoccupied states and the non-bonding O 2p states. For easier comparison, the O K-edge XAS spectra of the samples shown in Figures 2e, 3f, and 4e were rearranged in **Figure 6**a. The low $Fe^{3+/4+}$ oxidation voltage in LFMOF is directly reflected in the O K-edge spectra as a high-lying Fe^{4+} peak, which corresponds to a large charge transfer gap. This is contrasted with low-lying Fe^{4+} peaks in LFOF and LFTOF, which correspond to the high $Fe^{3+/4+}$ oxidation voltage and small charge transfer gap. The Fe^{4+} and Mn^{4+} peaks in the O K-edge spectra of LFMOF are indistinguishable, likely due to their superposition. Indeed, the $Fe^{3+/4+}$ and $Mn^{3+/4+}$ redox reactions in LFMOF occur almost simultaneously, suggesting an overlap of their redox energy levels. These distinct electronic states of Fe^{4+} between LFOF/LFTOF and LFMOF greatly influence their oxygen redox processes, leading to differing first-cycle Coulombic efficiency and voltage hysteresis behaviors. To fully elucidate this, we consider two key principles of the oxygen redox process discovered in prior studies: 1) Oxygen oxidation induces O–O dimerization (531 eV features in the O K-edge spectra, Figure 6a), which should occur through TM oxidation first followed by LMCT because of the kinetic difficulties of direct oxygen redox. For discharge, oxygen reduction occurs through TM reduction followed by metal-to-ligand charge transfer (MLCT).[22,23] 2) The magnitude of LMCT is strongly influenced by the charge transfer gap.[24] Given these principles, Figure 6b illustrates a schematic of the $Fe^{3+/4+}$ and $O^{2-/n-}$ redox processes in the different samples during the first cycle. On charging, the high-voltage $Fe^{3+/4+}$ OD-oxidation in LFOF and LFTOF creates empty Fe^{4+} bands that largely overlap with the non-bonding O 2p state. Due to the small charge transfer gap, Fe^{4+} is unstable against LMCT and O–O dimerization as part of the oxygen oxidation process, leading to a reduction back to Fe^{3+}. This significantly restricts the contribution of $Fe^{3+/4+}$ OD-oxidation to the charge capacity, resulting in excessive oxygen oxidation upon deep charging. The extent of oxygen oxidation is less in LFTOF than in LFOF because of the presence of LMCT-resistant low-voltage $Fe^{2+/3+}$ redox, which results in O_2 loss in LFOF but not in LFTOF (Figure S6, Supporting Information). In contrast to these two samples, the low-voltage $Fe^{3+/4+}$ OD-oxidation in LFMOF can be exten-

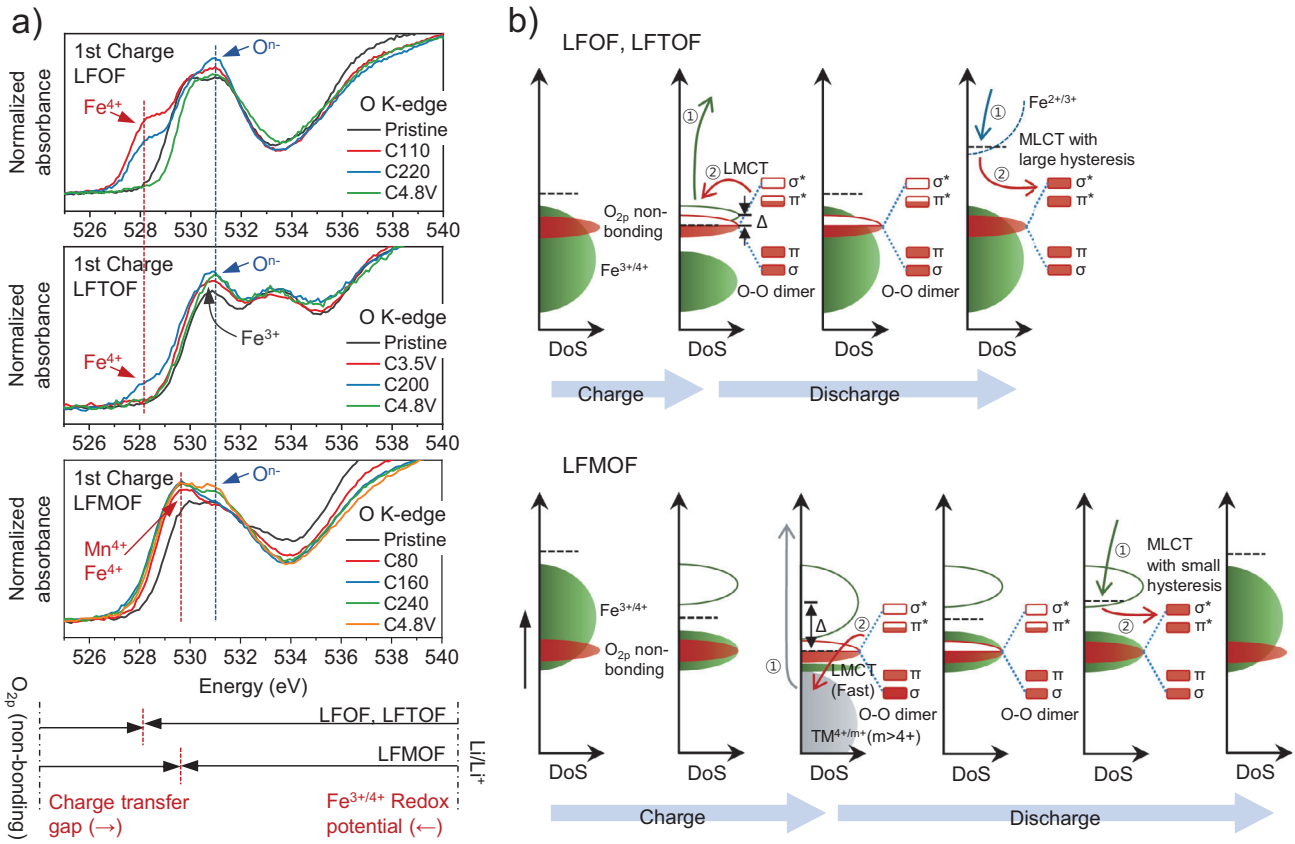

Figure 6. Characteristics of $Fe^{3+/4+}$ and $O^{2-/n-}$ redox processes in different samples and their relevance with first-cycle Coulombic efficiency and voltage hysteresis. a) Comparison of ex situ O K-edge XAS spectra of LFOF, LFTOF, and LFMOF electrodes during the first charge process. b) Schematic illustration of $Fe^{3+/4+}$ and $O^{2-/n-}$ redox processes in different samples during initial charge/discharge cycling (LFOF/LFTOF: upper, LFMOF: bottom).

sively utilized above the non-bonding O 2p state (bottom figures in Figure 6b). Although continuous $Fe^{3+/4+}$ OD-oxidation is followed by LMCT and O–O dimerization as part of the oxygen oxidation process, it may involve higher valent TM^{m+} ($m > 4+$) ions.[57] Note that due to the significantly negative charge transfer gap, TM^{m+} could spontaneously reduce to TM^{4+} through a fast LMCT, which could explain why the high-valent TM states are not observed experimentally. In LFMOF, most empty states of Fe^{4+} are positioned at a high energy level with a large charge transfer gap. Therefore, LMCT involving a reduction of Fe^{4+} is largely suppressed, as further confirmed by galvanostatic intermittent titration technique (GITT) experiments (Figure S15, Supporting Information). As a result, $Fe^{3+/4+}$ OD-redox (as well as $Mn^{3+/4+}$ redox) can be stably used in LFMOF without significant reduction during charging, preventing excessive oxygen oxidation. As summarized in Figure S16 (Supporting Information), the first-cycle Coulombic efficiency increases with the TM redox content that can resist LMCT during charging (i.e., in the order LFMOF > LFTOF > LFOF), because it can decrease the amount of resultant oxygen oxidation when the same state of charge is applied at the end of charge. The stability limit of the oxygen redox is roughly estimated to be the extraction of one Li per Li_2TMO_2F, irrespective of the compositions (i.e., it primarily depends on the oxygen oxidation content[24]; Figure S17, Supporting Information). That is, there is more safety margin for charge capacity in the order of LFMOF > LFTOF > LFOF. On discharge, $Fe^{4+/3+}$ OD-reduction first occurs before oxygen reduction takes place (i.e., redox inversion) in all the samples as a result of O–O dimerization, which causes a certain amount of inevitable voltage hysteresis.[24,35] However, the big difference between LFOF/LFTOF and LFMOF is that in LFOF/LFTOF, the oxygen reduction occurs after Fe^{4+} is fully reduced to Fe^{3+}, but it occurs in the middle of the $Fe^{4+/3+}$ (and $Mn^{4+/3+}$) reduction process in LFMOF. For LFOF/LFTOF, because the states in the $Fe^{3+/4+}$ redox energy level are already fully filled, electrons should first go to the empty states in the higher side $Fe^{2+/3+}$ redox energy level to reduce oxidized oxygen. This requires a large overpotential toward the low-voltage (i.e., high energy) side, further increasing voltage hysteresis. In contrast, for LFMOF, there are empty states in the $Fe^{3+/4+}$ (and $Mn^{3+/4+}$) redox energy level at the right position through which electrons can be transferred to the oxidized oxygen without a large overpotential. Therefore, the oxidized oxygen can be reduced at relatively high voltages, resulting in relatively small voltage hysteresis.

Altogether, it can be concluded that the modulation of the $Fe^{3+/4+}$ OD-redox potential to low voltages, which stabilizes Fe^{4+} against LMCT during charging and allows MLCT without large overpotential during discharging, plays a significant role in improving the first-cycle Coulombic efficiency and reducing voltage

hysteresis. This thereby enables the achievement of high energy density in Fe-based cathode materials. The question then arises about the origin of such voltage modulation in LFMOF. Previously, a combination of $Fe^{3+/4+}$ and $Mn^{3+/4+}$ redox couples has been used in $Na_{2/3}[Fe_{1/2}Mn_{1/2}]O_2$[58] and $Na_{0.77}Mn_{1/3}Fe_{2/3}O_2$[59] layered cathodes, but in those cases, the $Fe^{3+/4+}$ redox reaction occurred at ≈1 V higher than the $Mn^{3+/4+}$ redox reaction. Unlike the layered structure with TM—O—TM bonds with only ≈90° angle, the DRX structure can have TM—O—TM bonds with ≈180° angle in addition to the ≈90° one. The 180° angle, with an O ion directly bridging the e_g orbitals of Fe and Mn ions, may induce a very strong superexchange interaction[60,61] that lifts the electron energy level of the lower-energy-side redox couple (in the case of LFMOF, $Fe^{3+/4+}$),[4] resulting in voltage modulation. In addition, there could be another possible origin for voltage modulation. The DRX structure has diverse local environments, and the presence of TM ions that can absorb local distortion is known to contribute to lowering the energy of the structure.[62,63] While Mn^{3+} Jahn–Teller distortion can contribute to stabilizing the DRX structure by partially accommodating local distortions according to its distortion mode,[62,63] it can be anticipated to lose this function as it oxidizes to Mn^{4+}. Simultaneous oxidation of Mn^{3+} and Fe^{3+} provides another Jahn–Teller active Fe^{4+}, which could offset such effect, thereby stabilizing the DRX structure. This structural relaxation could also make $Fe^{3+/4+}$ oxidation energetically favorable at a lower voltage. Meanwhile, when comparing the electrochemical curves between LFMOF and its two endmembers, LFOF and Li_2MnO_2F (LMOF) (Figure S18, Supporting Information), it is observed that the combination of Fe^{3+} and Mn^{3+} has a synergetic effect in activating and stabilizing oxygen redox. This enables LFMOF to achieve the highest energy density among the three compounds. Although LFMOF demonstrated impressive energy density using only economically viable redox couples such as $Fe^{3+/4+}$, $Mn^{3+/4+}$, and $O^{2-/n-}$, further reduction in residual voltage hysteresis is required to enhance energy efficiency. The DRX structure provides a means to maximize non-hysteretic cationic redox while minimizing hysteretic oxygen redox thanks to its compositional flexibility, but oxygen redox is still necessary for boosting energy density. Completely solving the voltage hysteresis problem is a nontrivial task, as it may involve suppressing O–O dimerization that could be facilitated in a disordered structure with many local distortions.[27] Further studies on the characteristics of short-range order (SRO) may be necessary, as this has previously been shown to significantly affect the voltage hysteresis in the DRX cathode materials.[64]

3. Conclusion

In this paper, three different DRX oxyfluorides, LFOF, LFTOF, and LFMOF, were synthesized using a mechanochemical method to investigate the compositional effects on the reaction mechanism in Fe-based cathode materials. These materials exhibited distinct first-cycle Coulombic efficiency and voltage hysteresis behaviors, which were explained based on electrochemical and spectroscopic characterizations, as well as the theories of anionic redox. It was demonstrated that the redox potential of the $Fe^{3+/4+}$ couple can be lowered when combined with the $Mn^{3+/4+}$ redox couple in the DRX structure. This lowering of the redox potential contributes to the increased reversibility of the $Fe^{3+/4+}$ and $O^{2-/n-}$ redox processes. As shown in LFMOF, the OD-oxidation of $Fe^{3+/4+}$ occurring at a lowered voltage creates a moderately high charge transfer gap in the electronic structure. On charge, oxygen oxidation can occur through LMCT without reducing Fe^{4+} to Fe^{3+}. This stabilized $Fe^{3+/4+}$ OD-redox, along with the $Mn^{3+/4+}$ redox, reduces the total amount of oxygen redox thereby contributing to a high Coulombic efficiency. On discharge, a considerable amount of empty $Fe^{3+/4+}$ (and $Mn^{3+/4+}$) redox bands remain at a moderate energy level when oxygen reduction occurs. This allows for MLCT without a large overpotential, thereby enabling less hysteretic oxygen reduction. These findings demonstrated that Fe can be utilized as the main element in high energy density cathode materials with densely packed crystal frameworks, potentially achieving energy densities of 1000 Wh kg^{-1}.

4. Experimental Section

Synthesis: LFOF, LFTOF, and LFMOF compounds were synthesized via a mechanochemical ball-milling method. For LFOF, Li_2O (Alfa Aesar, 99.5%), LiF (Alfa Aesar, 99.98%), and Fe_2O_3 (Sigma–Aldrich, 99.7%) as starting precursors were used. For LFTOF, the precursors were Li_2O (Alfa Aesar, 99.5%), LiF (Alfa Aesar, 99.98%), FeO (Sigma–Aldrich, 99.8%), and TiO_2 (Sigma–Aldrich, 99.7%). In the case of LFMOF, the precursors included Li_2O (Alfa Aesar, 99.5%), LiF (Alfa Aesar, 99.98%), FeO (Sigma–Aldrich, 99.8%) and MnO_2 (Alfa Aesar, 99.9%). This study loaded a stoichiometric amount of the precursors (total 1 g) along with a 25 g mixture of 5 mm and 10 mm zirconia balls (weight ratio of ≈1:1) into an Ar-filled, homemade 45 mL stainless steel vial. The ball-milling was executed at 500 rpm for 40 h with a 5 min rest every 1 h, using a planetary mill (PULVERISETTE 6, Fritsch). In addition, LMOF compound via the same mechanochemical ball-milling method was also synthesized. The precursors were Li_2O (Alfa Aesar, 99.5%), LiF (Alfa Aesar, 99.98%), and Mn_2O_3 (Sigma–Aldrich, 99.4%). The ball-milling condition was the same as those used for above three materials.

Electrochemistry: The cathode electrode was crafted from a mixture of 70% active material, 20% carbon black, and 10% PTFE. Initially, 280 mg of the active material, 80 mg of carbon black, and roughly 9 g of 5 mm zirconia balls into an Ar-filled, homemade 45 mL stainless steel vial were loaded. This mixture was then ball-milled at 300 rpm for 3 h with a 5 min rest every 1 h, using a planetary mill (PULVERISETTE 6, Fritsch). Subsequently, the mixture was manually combined with PTFE for 20 min using a mortar and pestle, followed by rolling it into a free-standing film inside an Ar-filled glove box. CR2032 coin cells were assembled using the cathode film, a glass microfiber separator (Whatman GF/F), a Li foil anode, and an electrolyte of 1.3 M $LiPF_6$ in ethylene carbonate (EC): diethyl carbonate (DEC) solution (3:7 by volume) inside an Ar-filled glove box. The loading density of the cathode film was 5–8 mg cm^{-2}. For the GITT experiments, a trilayer polypropylene-polyethylene-polypropylene (PP/PE/PP) membrane separator (Celgard 2300) instead of a glass microfiber separator, as it showed less self-discharge during extended relaxation periods was used. Galvanostatic charge/discharge cycling tests were conducted using a battery cycler (WBCS3000S, Won-A Tech). The specific capacity and energy were calculated based on the weight of active materials in the cathode films.

Characterization: The XRD patterns were obtained using a diffractometer (D2 PHASER, Bruker) equipped with Cu Kα radiation (λ = 1.54184 Å) over a 2θ range of 10–90° with a step size of 0.01° and a step time of 5 s. An airtight sample holder to protect the samples from moist air was used. Rietveld refinement was performed using FullProf software. Hard XAS was conducted at the 10C-Wide XAFS and 7D-XAFS beamlines of PLS-II. For XAS measurements, the as-prepared powder and electrode samples were sealed with Kapton film to prevent contamination. Fe, Ti, and Mn K-edge spectra of the samples were recorded at

room temperature in transmission mode. In each measurement, the spectrum of a corresponding reference TM foil was simultaneously recorded. The hard XAS raw data were processed using the ATHENA software of IFEFFIT.[65] Energy calibration was accomplished using the first inflection points in the spectra of reference TM foils. To analyze the EXAFS region, R-space magnitude plots were generated by Fourier transforming the k^3 weighted $\chi(k)$ functions over a k range of 2–10 $Å^{-1}$ for the Fe and Mn K-edges. Nonlinear least-squares EXAFS fitting was performed using the ARTEMIS software of IFEFFIT[65] for the Fe and Mn K-edges. Theoretical functions, calculated using FEFF 6 code, were fitted to the experimental spectra in the R-space ranges corresponding to the first coordination shells (1–2 Å for the Fe and Mn K-edges). O and F K-edge soft XAS spectra were measured at the 2A-MS beamline of PLS-II. The samples were attached to an oxygen-free high-conductivity copper holder inside an Ar-filled glove box, transferred to the beamline in an airtight container, and quickly mounted on the spectrometer to minimize air exposure. Spectra in total electron yield (TEY) and FY modes were collected at room temperature. This study also recorded the spectrum of NiO powder as a reference. The soft XAS raw data were processed using the ATHENA software of IFEFFIT.[65] Energy calibration was completed using the spectrum of the NiO reference. ICP-AES analysis was conducted using an OPTIMA 8300 (Perkin-Elmer). SEM images were obtained using a JSM-IT800 (JEOL). For TEM measurement, as-prepared powders were dispersed in dimethyl carbonate (DMC) using a sonicator, then deposited onto an ultrathin carbon grid. The samples were prepared inside an Ar-filled glove box, and the resulting specimens were transferred to the TEM room in an airtight container. The specimens were then quickly mounted on a TEM (JEM-2100F, JEOL) to collect high-resolution TEM (HR-TEM) images, electron diffraction (ED) patterns, and EDS maps. A DEMS system was used to measure gas evolution during the charge and discharge processes. This system consists of a mass spectrometer (HPR-20 R&D, Hiden Analytical), a battery cycler (WBCS3000S, Won-A Tech), and a gas flow meter. To flow the gas generated inside the cell into the mass spectrometer, a modified 2032-coin cell with a 0.5 mm diameter hole at the cell bottom was used, and a mesh-type SUS current collector was employed. Each cell was assembled in an Ar-filled glovebox and left to relax for 2 h in Ar condition before the test. The electrochemical test was performed at a current density of 60 mA g^{-1} between 1.5 and 4.8 V. Then, the evolved gas immediately flowed into the mass spectrometer by the Ar carrier gas emitted at a rate of 15 cc min^{-1}.

Computational Details: All the DFT calculations were performed using the Vienna ab initio simulation package (VASP).[66] Projector-augmented wave (PAW) pseudopotentials[67] with a plane-wave basis set as implemented in VASP were utilized. Perdew–Burke–Ernzerhof (PBE) parametrization of the generalized gradient approximation (GGA)[68] was used for the exchange-correlation functional. For the DFT calculations, a $6 \times 3 \times 3$ k-point grid was used to calculate each structure. The GGA+U method[69] was adopted to address the localization of the *d*-orbital in Fe and Mn ions, with U values of 4.0 and 3.9 eV, as used in previous studies.[70,71] A kinetic energy cut-off of 500 eV was used in all the calculations, and all the structures were optimized until the force in the unit cell converged to within 0.03 eV $Å^{-1}$. CASM software was used to generate all the Li^+/vacancy configurations for each composition, followed by full DFT calculations on a maximum of 20 configurations with the lowest electrostatic energy for each composition.[72]

Supporting Information

Supporting Information is available from the Wiley Online Library or from the author.

Acknowledgements

This work was supported by the National Research Foundation of Korea (NRF) grant funded by the Korea government (MSIT) (No. NRF-2021M3H4A1A02045953 and No. NRF-2022R1A2B5B02002624).

Author Contributions

H.L. and W.-S.Y. conceived and designed the study. H.L. synthesized, characterized (XRD, XAS), and electrochemically tested the proposed compounds with help from M.K. and S.N. H.P. and J.K. conducted computational simulations and analyzed the data. Y.Y. and H.-D.L. performed the DEMS analyses. The manuscript was first written by H.L., and the computational part was added later by H.P. and J.K. It was then revised by W.-S.Y. with the help of other authors.

Conflict of Interest

The authors declare no conflict of interest.

Data Availability Statement

The data that support the findings of this study are available from the corresponding author upon reasonable request.

Keywords

Coulombic efficiency, disordered rock-salt, Fe-based cathodes, Li-ion batteries, oxygen redox, voltage hysteresis

Received: October 9, 2023
Revised: November 26, 2023
Published online: December 22, 2023

[1] L. Xie, C. Singh, S. K. Mitter, M. A. Dahleh, S. S. Oren, *Joule* **2021**, *5*, 1908.
[2] M. Li, J. Lu, Z. Chen, K. Amine, *Adv. Mater.* **2018**, *30*, 1800561.
[3] M. S. Whittingham, *Chem. Rev.* **2004**, *104*, 4271.
[4] A. K. Padhi, K. S. Nanjundaswamy, J. B. Goodenough, *J. Electrochem. Soc.* **1997**, *144*, 1188.
[5] J. Li, J. Li, J. Luo, L. Wang, X. He, *Int. J. Electrochem. Sci.* **2011**, *6*, 1550.
[6] M. M. Rahman, J.-Z. Wang, M. F. Hassan, S. Chou, Z. Chen, H. K. Liu, *Energy Environ. Sci.* **2011**, *4*, 952.
[7] L. Bordet-Le Guenne, P. Deniard, A. Lecerf, P. Biensan, C. Siret, L. Fournès, R. Brec, *J. Mater. Chem.* **1999**, *9*, 1127.
[8] S.-H. Wu, H.-Y. Liu, *J. Power Sources* **2007**, *174*, 789.
[9] J. Reimers, *Solid State Ionics* **1993**, *61*, 335.
[10] G. Prado, A. Rougier, L. Fourne'S, C. Delmas, *J. Electrochem. Soc.* **2000**, *147*, 2880.
[11] M. Tabuchi, Y. Nabeshima, K. Ado, M. Shikano, H. Kageyama, K. Tatsumi, *J. Power Sources* **2007**, *174*, 554.
[12] M. Tabuchi, Y. Nabeshima, M. Shikano, K. Ado, H. Kageyama, K. Tatsumi, *J. Electrochem. Soc.* **2007**, *154*, A638.
[13] J. Kikkawa, T. Akita, M. Tabuchi, K. Tatsumi, M. Kohyama, *J. Electrochem. Soc.* **2011**, *158*, A760.
[14] H. Shigemura, M. Tabuchi, H. Sakaebe, H. Kobayashi, H. Kageyama, *J. Electrochem. Soc.* **2003**, *150*, A638.
[15] M. Tabuchi, A. Nakashima, H. Shigemura, K. Ado, H. Kobayashi, H. Sakaebe, K. Tatsumi, H. Kageyama, T. Nakamura, R. Kanno, *J. Mater. Chem.* **2003**, *13*, 1747.
[16] N. Yabuuchi, M. Takeuchi, M. Nakayama, H. Shiiba, M. Ogawa, K. Nakayama, T. Ohta, D. Endo, T. Ozaki, T. Inamasu, K. Sato, S. Komaba, *Proc. Natl. Acad. Sci.* **2015**, *112*, 7650.
[17] N. Yabuuchi, M. Nakayama, M. Takeuchi, S. Komaba, Y. Hashimoto, T. Mukai, H. Shiiba, K. Sato, Y. Kobayashi, A. Nakao, M. Yonemura, K. Yamanaka, K. Mitsuhara, T. Ohta, *Nat. Commun.* **2016**, *7*, 13814.

[18] E. Mccalla, A. Abakumov, G. Rousse, M. Reynaud, M. T. Sougrati, B. Budic, A. Mahmoud, R. Dominko, G. Van Tendeloo, R. P. Hermann, J.-M. Tarascon, *Chem. Mater.* **2015**, *27*, 1699.
[19] E. Mccalla, M. T. Sougrati, G. Rousse, E. J. Berg, A. Abakumov, N. Recham, K. Ramesha, M. Sathiya, R. Dominko, G. Van Tendeloo, P. Novák, J.-M. Tarascon, *J. Am. Chem. Soc.* **2015**, *137*, 4804.
[20] C. Zhan, Z. Yao, J. Lu, L. Ma, V. A. Maroni, L. Li, E. Lee, E. E. Alp, T. Wu, J. Wen, Y. Ren, C. Johnson, M. M. Thackeray, M. K. Y. Chan, C. Wolverton, K. Amine, *Nat. Energy* **2017**, *2*, 963.
[21] H. Kobayashi, Y. Nakamura, M. Nakayama, S. Kodaki, R. Matsuo, I. Honma, *Adv. Energy Mater.* **2023**, *13*, 2203441.
[22] B. Li, M. T. Sougrati, G. Rousse, A. V. Morozov, R. Dedryvère, A. Iadecola, A. Senyshyn, L. Zhang, A. M. Abakumov, M.-L. Doublet, J.-M. Tarascon, *Nat. Chem.* **2021**, *13*, 1070.
[23] B. Li, K. Kumar, I. Roy, A. V. Morozov, O. V. Emelyanova, L. Zhang, T. Koç, S. Belin, J. Cabana, R. Dedryvère, A. M. Abakumov, J.-M. Tarascon, *Nat. Mater.* **2022**, *21*, 1165.
[24] M. Ben Yahia, J. Vergnet, M. Saubanère, M.-L. Doublet, *Nat. Mater.* **2019**, *18*, 496.
[25] R. A. House, G. J. Rees, M. A. Pérez-Osorio, J.-J. Marie, E. Boivin, A. W. Robertson, A. Nag, M. Garcia-Fernandez, K.-J. Zhou, P. G. Bruce, *Nat. Energy* **2020**, *5*, 777.
[26] D.-H. Seo, J. Lee, A. Urban, R. Malik, S. Kang, G. Ceder, *Nat. Chem.* **2016**, *8*, 692.
[27] J. Hong, W. E. Gent, P. Xiao, K. Lim, D.-H. Seo, J. Wu, P. M. Csernica, C. J. Takacs, D. Nordlund, C.-J. Sun, K. H. Stone, D. Passarello, W. Yang, D. Prendergast, G. Ceder, M. F. Toney, W. C. Chueh, *Nat. Mater.* **2019**, *18*, 256.
[28] M. Tabuchi, A. Nakashima, H. Shigemura, K. Ado, H. Kobayashi, H. Sakaebe, H. Kageyama, T. Nakamura, M. Kohzaki, A. Hirano, R. Kanno, *J. Electrochem. Soc.* **2002**, *149*, A509.
[29] Z. Lebens-Higgins, H. Chung, I. Temprano, M. Zuba, J. Wu, J. Rana, C. Mejia, M. A. Jones, L. Wang, C. P. Grey, Y. Du, W. Yang, Y. S. Meng, L. F. J. Piper, *Batteries Supercaps* **2021**, *4*, 771.
[30] J.-M. A. Mba, I. Arčon, G. Mali, E. Tchernychova, R. Witte, R. Kruk, M. Gaberšček, R. Dominko, *J. Power Sources* **2020**, *467*, 228230.
[31] J. Lee, A. Urban, X. Li, D. Su, G. Hautier, G. Ceder, *Science* **2014**, *343*, 519.
[32] A. Urban, J. Lee, G. Ceder, *Adv. Energy Mater.* **2014**, *4*, 1400478.
[33] R. Chen, S. Ren, M. Knapp, D. Wang, R. Witter, M. Fichtner, H. Hahn, *Adv. Energy Mater.* **2015**, *5*, 1401814.
[34] W. D. Richards, S. T. Dacek, D. A. Kitchaev, G. Ceder, *Adv. Energy Mater.* **2018**, *8*, 1701533.
[35] Q. Jacquet, A. Iadecola, M. Saubanère, H. Li, E. J. Berg, G. Rousse, J. Cabana, M.-L. Doublet, J.-M. Tarascon, *J. Am. Chem. Soc.* **2019**, *141*, 11452.
[36] B. Li, Z. Zhuo, L. Zhang, A. Iadecola, X. Gao, J. Guo, W. Yang, A. V. Morozov, A. M. Abakumov, J.-M. Tarascon, *Nat. Mater.* **2023**, *22*, 1370.
[37] M. Sathiya, G. Rousse, K. Ramesha, C. P. Laisa, H. Vezin, M. T. Sougrati, M.-L. Doublet, D. Foix, D. Gonbeau, W. Walker, A. S. Prakash, M. Ben Hassine, L. Dupont, J.-M. Tarascon, *Nat. Mater.* **2013**, *12*, 827.
[38] R. Kumar, R. J. Choudhary, M. W. Khan, J. P. Srivastava, C. W. Bao, H. M. Tsai, J. W. Chiou, K. Asokan, W. F. Pong, *J. Appl. Phys.* **2005**, *97*, 093526.
[39] S. Roychoudhury, R. Qiao, Z. Zhuo, Q. Li, Y. Lyu, J.-H. Kim, J. Liu, E. Lee, B. J. Polzin, J. Guo, S. Yan, Y. Hu, H. Li, D. Prendergast, W. Yang, *Energy Environ. Mater.* **2021**, *4*, 246.
[40] M. Abbate, F. M. F. De Groot, J. C. Fuggle, A. Fujimori, O. Strebel, F. Lopez, M. Domke, G. Kaindl, G. A. Sawatzky, M. Takano, Y. Takeda, H. Eisaki, S. Uchida, *Phys. Rev. B* **1992**, *46*, 4511.
[41] E. Mccalla, A. M. Abakumov, M. Saubanère, D. Foix, E. J. Berg, G. Rousse, M.-L. Doublet, D. Gonbeau, P. Novák, G. Van Tendeloo, R. Dominko, J.-M. Tarascon, *Science* **2015**, *350*, 1516.
[42] R. Sharpe, R. A. House, M. J. Clarke, D. Förstermann, J.-J. Marie, G. Cibin, K.-J. Zhou, H. Y. Playford, P. G. Bruce, M. S. Islam, *J. Am. Chem. Soc.* **2020**, *142*, 21799.
[43] R. Qiao, Y.-D. Chuang, S. Yan, W. Yang, *PLoS One* **2012**, *7*, e49182.
[44] Y. Ma, C. T. Chen, G. Meigs, K. Randall, F. Sette, *Phys. Rev. A* **1991**, *44*, 1848.
[45] W. E. Gent, K. Lim, Y. Liang, Q. Li, T. Barnes, S.-J. Ahn, K. H. Stone, M. Mcintire, J. Hong, J. H. Song, Y. Li, A. Mehta, S. Ermon, T. Tyliszczak, D. Kilcoyne, D. Vine, J.-H. Park, S.-K. Doo, M. F. Toney, W. Yang, D. Prendergast, W. C. Chueh, *Nat. Commun.* **2017**, *8*, 2091.
[46] B. Leedahl, D. A. Zatsepin, D. W. Boukhvalov, R. J. Green, J. A. Mcleod, S. S. Kim, E. Z. Kurmaev, I. S. Zhidkov, N. V. Gavrilov, S. O. Cholakh, A. Moewes, *J. Appl. Phys.* **2014**, *115*, 053711.
[47] D. A. Kitchaev, Z. Lun, W. D. Richards, H. Ji, R. J. Clément, M. Balasubramanian, D.-H. Kwon, K. Dai, J. K. Papp, T. Lei, B. D. Mccloskey, W. Yang, J. Lee, G. Ceder, *Energy Environ. Sci.* **2018**, *11*, 2159.
[48] J. Lee, D. A. Kitchaev, D.-H. Kwon, C.-W. Lee, J. K. Papp, Y.-S. Liu, Z. Lun, R. J. Clément, T. Shi, B. D. Mccloskey, J. Guo, M. Balasubramanian, G. Ceder, *Nature* **2018**, *556*, 185.
[49] I. I. Abate, C. D. Pemmaraju, S. Y. Kim, K. H. Hsu, S. Sainio, B. Moritz, J. Vinson, M. F. Toney, W. Yang, W. E. Gent, T. P. Devereaux, L. F. Nazar, W. C. Chueh, *Energy Environ. Sci.* **2021**, *14*, 4858.
[50] R. A. House, G. J. Rees, K. Mccoll, J.-J. Marie, M. Garcia-Fernandez, A. Nag, K.-J. Zhou, S. Cassidy, B. J. Morgan, M. Saiful Islam, P. G. Bruce, *Nat. Energy* **2023**, *8*, 351.
[51] A. E. Bocquet, A. Fujimori, T. Mizokawa, T. Saitoh, H. Namatame, S. Suga, N. Kimizuka, Y. Takeda, M. Takano, *Phys. Rev. B* **1992**, *45*, 1561.
[52] A. E. Bocquet, T. Mizokawa, T. Saitoh, H. Namatame, A. Fujimori, *Phys. Rev. B* **1992**, *46*, 3771.
[53] M. Imada, A. Fujimori, Y. Tokura, *Rev. Mod. Phys.* **1998**, *70*, 1039.
[54] E. Pavarini, E. Koch, J. van den Brink, G. Sawatzky, *Quantum Materials: Experiments and Theory*, Verlag des Forschungszentrum, Jülich **2016**.
[55] F. De Groot, A. Kotani, *Core Level Spectroscopy of Solids*, CRC press, Boca Raton, FL, USA **2008**.
[56] P. C. Rogge, R. U. Chandrasena, A. Cammarata, R. J. Green, P. Shafer, B. M. Lefler, A. Huon, A. Arab, E. Arenholz, H. N. Lee, T.-L. Lee, S. Nemšák, J. M. Rondinelli, A. X. Gray, S. J. May, *Phys. Rev. Mater.* **2018**, *2*, 015002.
[57] M. D. Radin, J. Vinckeviciute, R. Seshadri, A. Van Der Ven, *Nat. Energy* **2019**, *4*, 639.
[58] N. Yabuuchi, M. Kajiyama, J. Iwatate, H. Nishikawa, S. Hitomi, R. Okuyama, R. Usui, Y. Yamada, S. Komaba, *Nat. Mater.* **2012**, *11*, 512.
[59] B. Mortemard De Boisse, J.-H. Cheng, D. Carlier, M. Guignard, C.-J. Pan, S. Bordère, D. Filimonov, C. Drathen, E. Suard, B.-J. Hwang, A. Wattiaux, C. Delmas, *J. Mater. Chem. A* **2015**, *3*, 10976.
[60] J. Kanamori, *J. Phys. Chem. Solids* **1959**, *10*, 87.
[61] J. B. Goodenough, *Magnetism and the Chemical Bond*, Interscience, New York **1963**.
[62] A. Abdellahi, A. Urban, S. Dacek, G. Ceder, *Chem. Mater.* **2016**, *28*, 3659.
[63] A. Urban, A. Abdellahi, S. Dacek, N. Artrith, G. Ceder, *Phys. Rev. Lett.* **2017**, *119*, 176402.
[64] H. Lee, W. Choi, W. Lee, J.-H. Shim, Y.-M. Kim, W.-S. Yoon, *Adv. Energy Mater.* **2021**, *11*, 2002958.
[65] B. Ravel, M. Newville, *J. Synchrotron Rad.* **2005**, *12*, 537.
[66] G. Kresse, J. Furthmüller, *Comput. Mater. Sci.* **1996**, *6*, 15.
[67] P. E. Blöchl, *Phys. Rev. B* **1994**, *50*, 17953.

[68] J. P. Perdew, K. Burke, M. Ernzerhof, *Phys. Rev. Lett.* **1996**, *77*, 3865.
[69] I. A. Vladimir, F. Aryasetiawan, A. I. Lichtenstein, *J. Phys.: Condens. Matter* **1997**, *9*, 767.
[70] A. Jain, G. Hautier, S. P. Ong, C. J. Moore, C. C. Fischer, K. A. Persson, G. Ceder, *Phys. Rev. B* **2011**, *84*, 045115.
[71] Y. Wang, J. Liu, B. Lee, R. Qiao, Z. Yang, S. Xu, X. Yu, L. Gu, Y.-S. Hu, W. Yang, K. Kang, H. Li, X.-Q. Yang, L. Chen, X. Huang, *Nat. Commun.* **2015**, *6*, 6401.
[72] A. Van Der Ven, J. C. Thomas, Q. Xu, J. Bhattacharya, *Math. Comput. Simul.* **2010**, *80*, 1393.

